scientific reports

Check for updates

OPEN

Quasi-exact solutions for guided modes in two-dimensional materials with tilted Dirac cones

R. A. Ng[1], A. Wild[2], M. E. Portnoi[2,3] & R. R. Hartmann[1]✉

We show that if the solutions to the (2+1)-dimensional massless Dirac equation for a given one-dimensional (1D) potential are known, then they can be used to obtain the eigenvalues and eigenfunctions for the same potential, orientated at an arbitrary angle, in a 2D Dirac material possessing tilted, anisotropic Dirac cones. This simple set of transformations enables all the exact and quasi-exact solutions associated with 1D quantum wells in graphene to be applied to the confinement problem in tilted Dirac materials such as 8-*Pmmn* borophene. We also show that smooth electron waveguides in tilted Dirac materials can be used to manipulate the degree of valley polarization of quasiparticles travelling along a particular direction of the channel. We examine the particular case of the hyperbolic secant potential to model realistic top-gated structures for valleytronic applications.

It can be shown using supersymmetric methods that whenever the Schrödinger equation can be solved exactly for a one-dimensional (1D) potential, there exists a corresponding potential for which the two-dimensional (2D) Dirac equation admits exact eigenvalues and eigenfunctions[1]. A broad class of quasi-1D potentials can also be solved quasi-exactly by transforming the 2D Dirac equation into the Heun equation[2] or one of its confluent forms[3–5], or via the application of Darboux transformations[6–11]. These exact and quasi-exact bound-state solutions have direct applications to electronic waveguides in 2D Dirac materials[2–5,12,13], such as graphene, where the low-energy spectrum of the charge carriers can be described by a Dirac Hamiltonian[14], and the guiding potential can be generated via a top gate[15–20]. Recent advances in device fabrication, utilizing carbon nanotubes as top gates, has enabled the detection of individual guided modes[21], opening the door to several new classes of devices such as THz emitters[5,13], transistors[12], and ultrafast electronic switching devices[22]. These advances in electron waveguide fabrication technology make the need for analytic solutions all the more important, since they are highly useful in: determining device geometry, finding the threshold voltage required to observe a zero-energy mode[12], calculating the size of the THz pseudogap in bipolar waveguides[13], as well as ascertaining the optical selection rules[5,13] in graphene heterostructures.

In extension to the well-known case of graphene, Dirac cones can in general possess valley-dependent tilt[23]. There are only a handful of 2D electronic systems that have been predicted to host these tilted cones[24–33], one of which is 8-*Pmmn* borophene[23,34], which has attracted considerable attention. In general, boron-based nanomaterials are a growing field of interest[35–37]; indeed, exploring the tilt of 2D Dirac cones in the context of 8-*Pmmn* borophene has recently led to a plethora of theoretical works spanning many fields of research[38–84] from optics to transport, and many more; for a comprehensive review, see Ref.[85]. The spectacular rise of borophene, and the growing interest in tilted Dirac materials, has led to the revisiting of several well-known problems in graphene, e.g., Klein tunneling[47] and transport across quasi-1D heterostructures[43,52,73,86], within the context of tilted Dirac materials. As mentioned previously, methods such as supersymmetry and reducing the Dirac equation to the Heun equation, utilize solutions of known problems, to generate solutions to new ones. This begs the question: does a simple mapping exist which would allow us to harness the large body of exact and quasi-exact solutions for 1D waveguides in graphene and then apply them to materials with tilted Dirac cones?

In what follows, we show that the differential equations governing guided modes in an anisotropic tilted Dirac waveguide (orientated at an arbitrary angle) can, via a simple transformation, be mapped onto the graphene problem, i.e., transformed into the massless 2D Dirac equation[14], for the *same* potential, but of modified strength, effective momentum, and modified energy scale. After outlining the transformation, we study the particular case of the hyperbolic secant potential, which in graphene is known to admit quasi-exact solutions to the eigenvalue problem; but nevertheless, the whole spectrum can be obtained via a semi-analytic approach[2,12]. We use this

[1]Physics Department, De La Salle University, 2401 Taft Avenue, 0922 Manila, Philippines. [2]Physics and Astronomy, University of Exeter, Stocker Road, Exeter EX4 4QL, UK. [3]ITMO University, St. Petersburg, Russia 197101. ✉email: Richard.hartmann@dlsu.edu.ph

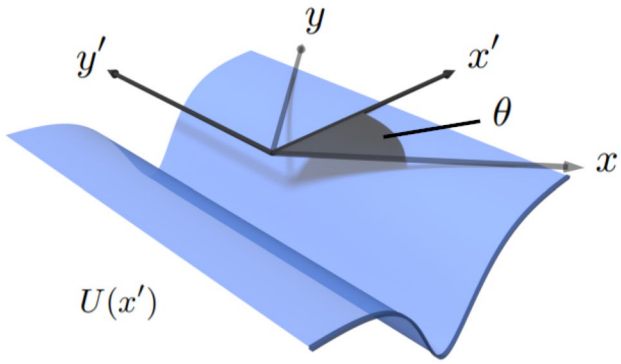

Figure 1. A schematic diagram of an electrostatic potential, $U(x')$, created by an applied top-gate voltage in a tilted 2D Dirac material. The waveguide is orientated at an angle of θ, relative to the x-axis of the crystal. The potential is invariant along the y'-axis, and varies in strength along the x'-axis. The $x' - y'$ axes are denoted by the solid black arrows, whereas the crystallographic axes $x - y$ are shown by the light gray arrows.

known graphene waveguide spectrum to generate the corresponding tilted waveguide spectrum, which is verified using a transfer matrix method. Finally, we discuss valleytronic applications.

Transformation

The Hamiltonian describing the guided modes contained within a smooth electron waveguide in a tilted Dirac material can be written as

$$\hat{H} = \hbar\left(v_x\sigma_x\hat{k}_x + sv_y\sigma_y\hat{k}_y + sv_t\sigma_0\hat{k}_y\right) + \sigma_0 U(x,y), \tag{1}$$

where $\hat{k}_x = -i\partial_x, \hat{k}_y = -i\partial_y, \sigma_{x,y}$ are the Pauli spin matrices, σ_0 is the identity matrix, v_x and v_y are the anisotropic velocities, v_t is the tilt velocity and $s = \pm 1$ is the valley index number; here $s = 1$ and $s = -1$ are analogous to the K and K' valley, respectively. This Hamiltonian is of the same form as the low-energy two-band effective Hamiltonian used to describe 8-*Pmmn* borophene[23], 2*B*:*Pmmn* borophane[87], and α-(BEDT-TTF)$_2$I$_3$[24,25]. In what follows, we set $s = 1$, but it should be noted that the other valley's eigenvalues can be obtained by replacing v_y and v_t with $-v_y$ and $-v_t$. In general, the crystallographic orientation is not known, nor is it currently possible to deposit the top gate at a selected angle relative to the crystallographic axis. Therefore, we shall solve for the case of a waveguide at an arbitrary angle relative to the crystallographic axis $(x - y)$. The electrostatic potential, $U(x,y)$, is 1D, directed along the y'-axis, and varies along the x'−axis (see Fig. 1 for geometry), i.e., $U = U(x')$. We rotate the $x - y$ axes counterclockwise through an angle θ. The new axes $x' - y'$ are defined by the original coordinates via the transformation:

$$\begin{aligned} x' &= x\cos\theta + y\sin\theta, \\ y' &= -x\sin\theta + y\cos\theta. \end{aligned} \tag{2}$$

Hence, the wave vector operators in the non-rotated coordinate system $\hat{k} = \left(\hat{k}_x, \hat{k}_y\right)$ are expressed in the rotated coordinate frame, $\hat{k}' = \left(\hat{k}_{x'}, \hat{k}_{y'}\right)$, via the relations:

$$\begin{aligned} \hat{k}_x &= \cos\theta\hat{k}_{x'} - \sin\theta\hat{k}_{y'}, \\ \hat{k}_y &= \sin\theta\hat{k}_{x'} + \cos\theta\hat{k}_{y'}. \end{aligned} \tag{3}$$

The Hamiltonian, Eq. (1), acts on the two-component Dirac wavefunction $\Psi = \left(\psi_A(x'),\ \psi_B(x')\right)^{\mathsf{T}} e^{ik_{y'}y'}$ to yield the coupled first-order differential equations $\hat{H}\Psi = \varepsilon\Psi$, where ψ_A and ψ_B are the wavefunctions associated with the A and B sublattices of the tilted Dirac material. These coupled first-order differential equations can be recast into the same equations used to describe guided modes propagating along a smooth electron waveguide in graphene:

$$\left(\sigma_x\hat{k}_{x'} + \sigma_y\widetilde{\Delta} + \sigma_0\widetilde{V}(x')\right)\Phi(x') = \widetilde{E}\Phi(x'), \tag{4}$$

where the effective potential $\widetilde{V}$, energy $\widetilde{E}$, and momentum $\widetilde{\Delta}$ are obtained from the original tilted case via the relations:

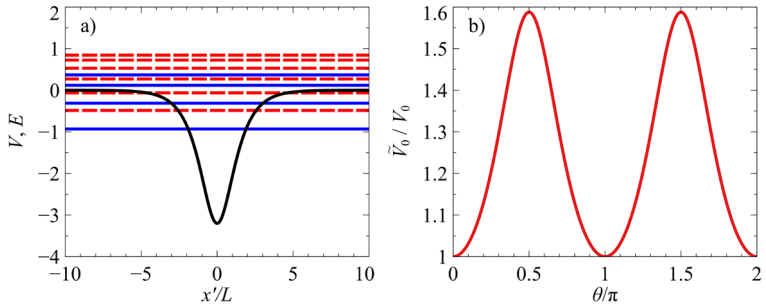

Figure 2. (**a**) The black curve shows the hyperbolic secant potential $V(x') = -V_0/\cosh(x'/L)$, for the case of $V_0 = 3.2$. The dashed and solid horizontal lines are the bound-state energy levels for the $s = 1$ and $s = -1$ chirality, respectively (which corresponds to the K and K' valley in the effective graphene sheet), for the case of $\Delta = k_{y'}L = 1$, when the waveguide is orientated at angle $\theta = 0$. The tilted Dirac material is defined by parameters $v_x = 0.86\, v_F$, $v_y = 0.69\, v_F$ and $v_t = 0.32\, v_F$. (**b**) The relative strength of the effective potential's depth, $\widetilde{V}_0$, compared to the actual potential depth V_0.

$$\begin{aligned}\widetilde{V}(x') &= \frac{lV(x')}{l^2 - t^2\sin^2\theta},\\ \widetilde{E} &= \frac{l}{l^2 - t^2\sin^2\theta}\left(E - \frac{t\cos\theta}{l^2}\Delta\right),\\ \widetilde{\Delta} &= \frac{T\Delta}{l\sqrt{l^2 - t^2\sin^2\theta}},\end{aligned} \tag{5}$$

where $V(x') = U(x')L/\hbar v_x$, $E = \varepsilon L/\hbar v_x$ and $\Delta = k'_y L$, and L is a constant, associated with the effective width of the potential. We define the tilt and anisotropy parameters as $t = v_t/v_x$ and $T = v_y/v_x$, respectively, and $l = \sqrt{1 - (1 - T^2)\sin^2\theta}$. The eigenfunctions of the guided modes in the effective graphene sheet, Φ, can be mapped onto the tilted Dirac spinor components, ψ_A and ψ_B, via the expression:

$$\Phi(x') = \begin{pmatrix}(1+\mu)\psi_A + (1-\mu)\psi_B e^{-i\varphi}\\ (1-\mu)\psi_A + (1+\mu)\psi_B e^{-i\varphi}\end{pmatrix} e^{-i\sin\theta\int \frac{t(V-E)+k_{y'}\left(1+t^2-T^2\right)\cos\theta}{l^2-t^2\sin^2\theta}dx'}, \tag{6}$$

where $\varphi = \arctan(T\tan\theta)$ and $\mu = (l - t\sin\theta)^{\frac{1}{2}}(l + t\sin\theta)^{-\frac{1}{2}}$. It then follows that if the eigenfunctions and eigenvalues are known for the potential $\widetilde{V}$ in graphene, one can immediately write down the eigenfunctions and eigenvalues of a 1D confining potential of the same form, orientated at an arbitrary angle, in a tilted Dirac material. Conversely, if a quasi-1D potential readily admits exact or quasi-exact solutions for the tilted case, and no solutions are known for the graphene problem, then our mapping method can be used to obtain the eigenfunctions and eigenvalues for the case of graphene. This mapping also reveals the angular dependence of the number of guided modes contained within the waveguide. Namely, it can be seen from Eq. (5) that rotating the orientation of the waveguide is equivalent to varying the effective depth of the potential (see Fig. 2b). Indeed, the effective potential's depth, $\widetilde{V}_0$, is equal to the actual potential's depth, V_0 at $\theta = 0$ and rises to a maximum value of $\widetilde{V}_0/V_0 = T/(T^2 - t^2)$ at $\theta = \pi/2$.

It should be noted that to perform the same transformations for the other chirality (i.e., the $s = -1$, or graphene K' valley analog), one must exchange t with $-t$, and T with $-T$. Therefore, the eigenvalue spectrum of one valley can be obtained by a reflection of the other valley's eigenvalue spectrum about the $k_{y'}$-axis. It can be seen from Eq. (5) that in the absence of a tilt term, i.e., $t = 0$, the eigenvalue spectrum of a given valley is symmetric with respect to $k_{y'}$. Thus, both chiralities have the same band structure. Similarly for $t \neq 0$, if the waveguide is orientated such that $\cos\theta = 0$, the eigenvalue spectrum is chirality-independent. In all other cases, the energy spectrum for a given valley lacks $E(k_{y'}) = E(-k_{y'})$ symmetry. This gives rise to the possibility of utilizing smooth electron waveguides in tilted Dirac materials as the basis of valleytronic devices. This will be discussed in the penultimate section.

Quasi-exact solution to the tilted Dirac equation for the hyperbolic secant potential

In this section, we shall apply our simple transformations, given in Eq. (5), to generate the energy spectrum of a smooth electron waveguide in a tilted Dirac material for a potential which has been studied in depth in graphene[2,12]:

$$V(x') = -\frac{V_0}{\cosh(x'/L)}. \tag{7}$$

This potential, shown in Fig. 2a, belongs to the class of quantum models which are quasi-exactly solvable[2,88–94], where only some of the eigenfunctions and eigenvalues are found explicitly. The depth of the well is given by V_0,

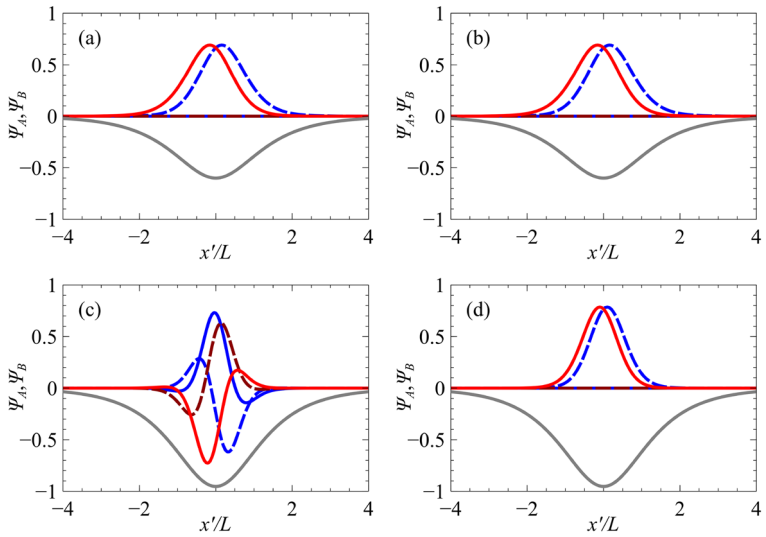

Figure 3. The normalized zero-energy state (lowest positive momentum) wavefunctions of the hyperbolic secant potential, $V(x') = -V_0/\cosh(x'/L)$, of strength $V_0 = -3.2$ and orientation: (**a**) $\theta = 0$ and (**c**) $\theta = \pi/2$ in a tilted Dirac material defined by parameters $v_x = 0.86\, v_F$, $v_y = 0.69\, v_F$ and $v_t = 0.32\, v_F$, for the $s = 1$ chirality, i.e., the K valley in the effective graphene sheet. The corresponding wavefunctions of the effective graphene waveguide are given in panels (**b**) and (**d**). The solid red and blue lines correspond to the real part of ψ_A and ψ_B respectively, while the dashed lines correspond to their imaginary parts. The grey line shows the potential as a guide to the eye.

and the potential width is characterized by the parameter L. Here V_0 and L are taken to be positive parameters. For realistic top-gated structures, the width of the potential is defined by the geometry of the top gate structure, and the strength of the potential is defined by the voltage applied to the top gate. In graphene, the wavefunctions can be solved in terms of Heun polynomials, which reduce to hypergeometric functions for the case of zero energy[2,12]. For zero-energy modes ($\widetilde{E} = 0$), the permissible values of $\widetilde{\Delta}$ are given by the simple relation $\widetilde{\Delta} = \widetilde{V}_0 - n - \frac{1}{2}$, where $\widetilde{V}_0$ is the depth of the effective potential and n is a non-negative integer. For non-zero energies, exact energy eigenvalues can be obtained when the Heun polynomials are terminated[2]. To illustrate the power of our mapping method, we apply the transformations given in Eq. (5) to the well-known zero-energy solutions to the 2D Dirac equation for the 1D hyperbolic secant potential. The corresponding tilted Dirac equation solutions become:

$$E = \frac{t\cos\theta}{T\sqrt{l^2 - t^2\sin^2\theta}}\left[V_0 - \left(n + \frac{1}{2}\right)\frac{l^2 - t^2\sin^2\theta}{l}\right], \tag{8}$$

and their corresponding $n = 0$ eigenfunctions for two different waveguide orientations are shown in Fig. 3, for the case of 8-*Pmmn* borophene, which is described by the parameters $v_x = 0.86\, v_F$, $v_y = 0.69\, v_F$ and $v_t = 0.32\, v_F$[23].

In Fig. 4 we plot the 8-*Pmmn* borophene eigenvalue spectrum for the potential defined by $V_0 = 3.2$ for two orientations, $\theta = 0$ and $\theta = \pi/2$, as well as the graphene waveguide spectra (quasi-analytically determined[2]) used in the mapping. In the same figure, we also plot the numerical solutions to the tilted Dirac problem obtained via a transfer matrix method (see Supplementary Material). We show in blue crosses the exact solutions given in Eq. (8) together with the complete set of mapped quasi-exact solutions given in Ref.[2]. It can be seen from Fig. 4 that the waveguide orientated at $\theta = \pi/2$ contains more bound states than the waveguide orientated at $\theta = 0$. This is a result of the effective graphene potential being deeper, and thus supporting more guided modes. It should be noted that for potentials which vanish at infinity, i.e., $V(\pm\infty) = E = 0$, only the zero-energy modes are truly confined, since the density of states vanishes outside of the well. Guided modes occurring at non-zero energies can always couple to continuum states outside of the well, thus having a finite lifetime.

Valleytronic applications

It has been suggested that the valley quantum number can be used as a basis for carrying information in graphene-based devices[95] in an analogous manner to spin in semiconductor spintronics[96,97]. Unlike in the case of graphene (in the conical regime), smooth electrostatic potentials in tilted Dirac materials can be utilized as a means to achieve valley polarization. The majority of studies have focused on tunneling across electrostatically-induced potential barriers, and valley filtering and beam splitting have been demonstrated[43,47,52,73,86]. It has also been shown that the allowed transmission angles through a potential can be controlled using magnetic barriers[86]. We propose a change in geometry: rather than studying chirality-dependent transmission across barriers, we shift the focus to studying guided modes along quasi-1D confining potentials. The conductance along such a channel can be measured by placing one terminal at each end. According to the Landauer formula, when the Fermi level is set to energy E (by modulating the back-gate voltage[21]), the conductance along the waveguide is

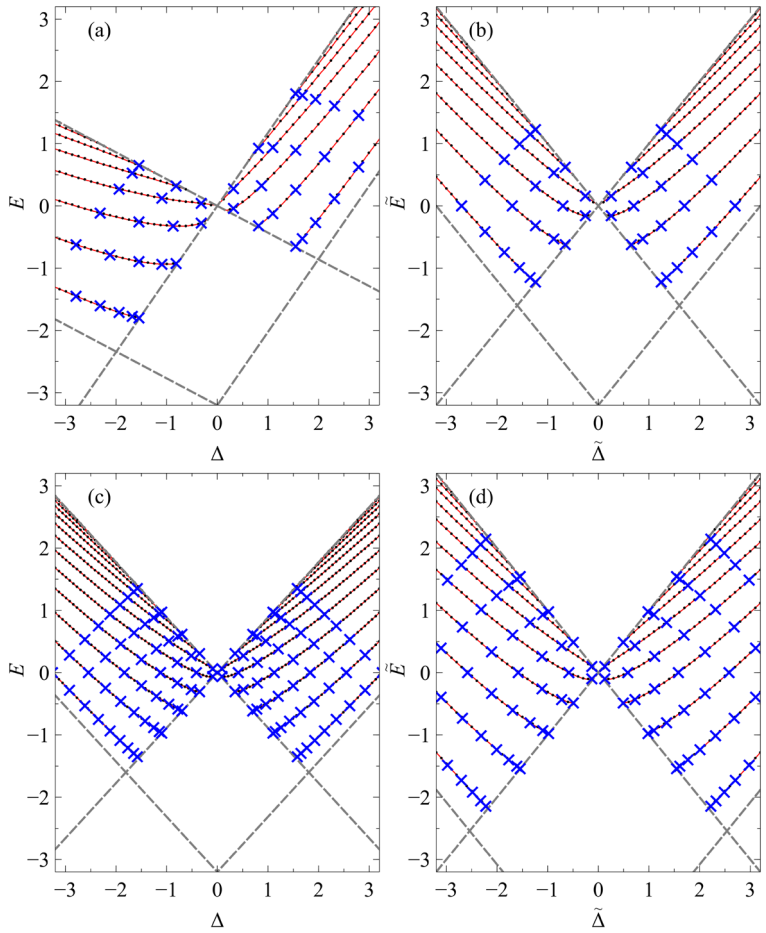

Figure 4. The energy spectrum of confined states (for the $s = 1$ chirality, i.e., the K valley in the effective graphene sheet) in the hyperbolic secant potential $V(x') = -V_0/\cosh(x'/L)$, of strength $V_0 = 3.2$, as a function of dimensionless momentum along the waveguide, $\Delta = k'_y L$, for the orientations (**a**) $\theta = 0$ and (**c**) $\theta = \pi/2$ in a tilted Dirac material, defined by parameters $v_x = 0.86\, v_F$, $v_y = 0.69\, v_F$ and $v_t = 0.32\, v_F$. The energy spectra of the effective graphene waveguide from whence they came, are given in panels (**b**) and (**d**), respectively. The black dots denote the semi-analytic eigenvalues, the blue crosses represent the quasi-exact eigenvalues, and the solid red lines show the eigenvalues numerically obtained via a transfer matrix method. The boundary at which the bound states merge with the continuum is denoted by the grey dashed lines.

simply $2(n_K + n_{K'})e^2/h$, where n_K and $n_{K'}$ are the number of modes belonging to the $s = 1$ and $s = -1$ chirality, respectively (or the K and K' valley in the effective graphene sheet), at that particular energy.

In a 2D Dirac material subject to a quasi-1D potential, the introduction of the tilt parameter breaks the $E(\Delta) = E(-\Delta)$ symmetry for a given valley. Indeed, for a given valley, the additional tilt term increases the particle velocity along one direction of the barrier and decreases it along the opposite direction; and vice versa for the other valley. For the case of type-I Dirac materials, i.e., $t < T$, it can be seen from Fig. 5 that for a given sign of Δ, the eigenvalues of the critical solutions (sometimes referred to as the zero-momentum solutions: i.e., bound states with energy $|E| = |\Delta|$) belonging to the two valleys are different. Thus, providing that $t \neq 0$ and $\cos\theta \neq 0$, there exists a range of energies for which there will be more bound states propagating along a particular direction belonging to one valley than the other, i.e., valley polarization. The degree of valley polarization can be controlled by varying the strength of the electrostatic potential and by changing the position of the Fermi level, which in practical devices is achieved by modulating the back-gate voltage[21]. Full valley polarization can be achieved for energies less than the lowest-lying supercritical state (defined as a bound state with energy $E = -\Delta$) belonging to the valley where the tilt term enhances the particle's velocity, indicated by the shaded region in Fig. 5. However, although full valley polarization along a particular direction can be realized, to generate a valley-polarized current one must lift the $y' = -y'$ symmetry. This can be achieved by applying an in-plane electric field along the waveguide.

For type-III tilted Dirac materials, i.e., $t = T$, full valley polarization occurs for all energies and all orientations of the waveguide. For such materials the infinite number of positive-energy critical solutions of graphene map onto the zero-energy modes of a type-III Dirac material. Consequently, the infinitely many zero-energy modes will give rise to a sharp peak in the conductance along the channel when the Fermi energy is in the proximity of $E = 0$. This is in stark contrast to the case of graphene, where the creation of an infinite number of zero-energy

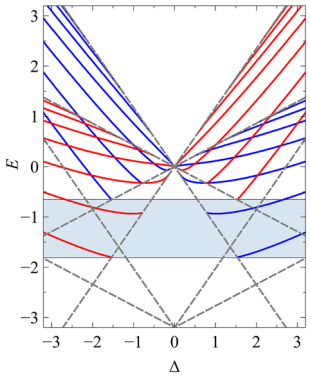

Figure 5. The energy spectrum of confined states in the hyperbolic secant potential $V(x') = -V_0/\cosh(x')$, of strength $V_0 = 3.2$, as a function of Δ for the $s = 1$ and $s = -1$ chirality (i.e., the K and K' valley in the effective graphene sheet), depicted by the red and blue lines, respectively. The waveguide is orientated at $\theta = 0$ and the tilted Dirac material is defined by parameters $v_x = 0.86\, v_F$, $v_y = 0.69\, v_F$ and $v_t = 0.32\, v_F$. The boundary at which the bound states merge with the continuum is denoted by the grey dashed lines. The shaded area represents the energy range for which full valley polarization can be achieved for a given value of Δ.

states requires an infinitely deep and wide potential[4,98–101]. Since the potential possesses infinitely many bound states, which infinitely accumulate at $E = 0$, a type-III Dirac material could be used as a THz emitter; namely, the Fermi level could be set below $E = 0$, and optical photons can be absorbed from low-lying energy levels to $E = 0$. Then the photo-excited carriers can relax back down to the Fermi level via the emission of THz photons through the closely spaced energy levels in the proximity of zero energy.

Lastly, for type-II tilted Dirac materials, i.e., $t > T$, full valley polarization occurs for all energies; however, bound states occur only for orientations within the range $-1/\sqrt{t^2 - T^2} < \tan(\theta + n\pi) < 1/\sqrt{t^2 - T^2}$. In the limit at which θ becomes imaginary, i.e., the boundary at which the equi-energy surfaces become unbounded, the effective potential required for mapping diverges.

Conclusion

We have shown that if the eigenvalues and eigenfunctions of a quasi-1D potential in graphene are known, then they can be used to obtain the corresponding results for the same potential (with modified strength, orientated at arbitrary angle), for a 2D Dirac material hosting anisotropic, tilted Dirac cones. Therefore, all the rich physics associated with guiding potentials in graphene, e.g., THz pseudogaps in bipolar waveguides, can be revisited in the context of tilted Dirac materials, but with the distinct advantage of knowing the eigenvalues and eigenfunctions. We have also shown that in stark contrast to smooth electron waveguides in graphene, valley degeneracy can be broken in tilted 2D Dirac materials for a broad range of waveguide orientations, anisotropy and tilt parameters. The degree of valley polarization along the waveguide can be controlled by varying the potential strength of the top gate, and also by changing the back-gate voltage. Tilted 2D Dirac materials, such as 8-*Pmmn* borophene, are therefore promising building blocks for tunable valleytronic devices.

Methods

The Supplementary Information contains a full description of the transfer matrix method used to calculate the band structure of guiding potentials in 2D Dirac materials with tilted Dirac cones.

Data availibility

This study did not generate any new data. The datasets used and analysed in this study are available from the corresponding author upon request.

Received: 15 November 2021; Accepted: 28 April 2022
Published online: 10 May 2022

References

1. Cooper, F., Khare, A., Musto, R. & Wipf, A. Supersymmetry and the Dirac equation. *Ann. Phys.* **187**, 1–28. https://doi.org/10.1016/0003-4916(88)90279-5 (1988).
2. Hartmann, R. R. & Portnoi, M. E. Quasi-exact solution to the Dirac equation for the hyperbolic-secant potential. *Phys. Rev. A* **89**, 012101. https://doi.org/10.1103/physreva.89.012101 (2014).
3. Downing, C. A. & Portnoi, M. E. One-dimensional Coulomb problem in Dirac materials. *Phys. Rev. A* **90**, 052116. https://doi.org/10.1103/PhysRevA.90.052116 (2014).
4. Hartmann, R. R. & Portnoi, M. E. Two-dimensional Dirac particles in a Pöschl–Teller waveguide. *Sci. Rep.* **7**, 1–10. https://doi.org/10.1038/s41598-017-11411-w (2017).
5. Hartmann, R. R. & Portnoi, M. E. Guided modes and terahertz transitions for two-dimensional Dirac fermions in a smooth double-well potential. *Phys. Rev. A* **102**, 052229. https://doi.org/10.1103/physreva.102.052229 (2020).

6. Schulze-Halberg, A. & Ojel, M. Darboux transformations for the massless Dirac equation with matrix potential: Construction of zero-energy states. *Eur. Phys. J. Plus* **134**, 1–12. https://doi.org/10.1140/epjp/i2019-12460-2 (2019).
7. Schulze-Halberg, A. Higher-order Darboux transformations for the massless Dirac equation at zero energy. *J. Math. Phys.* **60**, 073505. https://doi.org/10.1063/1.5095151 (2019).
8. Schulze-Halberg, A. Arbitrary-order Darboux transformations for two-dimensional Dirac equations with position-dependent mass. *Eur. Phys. J. Plus* **135**, 1–13. https://doi.org/10.1140/epjp/s13360-020-00345-4 (2020).
9. Schulze-Halberg, A. Higher-order Darboux transformations for the Dirac equation with position-dependent mass at nonvanishing energy. *Eur. Phys. J. Plus* **135**, 1–14. https://doi.org/10.1140/epjp/s13360-020-00882-y (2020).
10. Schulze-Halberg, A. & Roy, P. Dirac systems with magnetic field and position-dependent mass: Darboux transformations and equivalence with generalized Dirac oscillators. *Ann. Phys.* **431**, 168534. https://doi.org/10.1016/j.aop.2021.168534 (2021).
11. Schulze-Halberg, A. First-order Darboux transformations for Dirac equations with arbitrary diagonal potential matrix in two dimensions. *European Physical Journal Plus* **136**, 1–18. https://doi.org/10.1140/epjp/s13360-021-01804-2 (2021).
12. Hartmann, R. R., Robinson, N. J. & Portnoi, M. E. Smooth electron waveguides in graphene. *Phys. Rev. B* **81**, 245431. https://doi.org/10.1103/physrevb.81.245431 (2010).
13. Hartmann, R. R. & Portnoi, M. E. Bipolar electron waveguides in graphene. *Phys. Rev. B* **102**, 155421. https://doi.org/10.1103/PhysRevB.102.155421 (2020).
14. Castro Neto, A. H., Guinea, F., Peres, N. M. R., Novoselov, K. S. & Geim, A. K. The electronic properties of graphene. *Rev. Mod. Phys.* **81**, 109–162. https://doi.org/10.1103/RevModPhys.81.109 (2009).
15. Huard, B. *et al.* Transport measurements across a tunable potential barrier in graphene. *Phys. Rev. Lett.* **98**, 236803. https://doi.org/10.1103/PhysRevLett.98.236803 (2007).
16. Özyilmaz, B. *et al.* Electronic transport and quantum Hall effect in bipolar graphene $p-n-p$ junctions. *Phys. Rev. Lett.* **99**, 166804. https://doi.org/10.1103/PhysRevLett.99.166804 (2007).
17. Liu, G., Velasco, J., Bao, W. & Lau, C. N. Fabrication of graphene $p-n-p$ junctions with contactless top gates. *Appl. Phys. Lett.* **92**, 203103. https://doi.org/10.1063/1.2928234 (2008).
18. Gorbachev, R. V., Mayorov, A. S., Savchenko, A. K., Horsell, D. W. & Guinea, F. Conductance of $p-n-p$ graphene structures with "air-bridge" top gates. *Nano Lett.* **8**, 1995–1999. https://doi.org/10.1021/nl801059v (2008).
19. Williams, J., Low, T., Lundstrom, M. & Marcus, C. Gate-controlled guiding of electrons in graphene. *Nat. Nanotechnol.* **6**, 222–225. https://doi.org/10.1038/nnano.2011.3 (2011).
20. Rickhaus, P. *et al.* Guiding of electrons in a few-mode ballistic graphene channel. *Nano Lett.* **15**, 5819–5825. https://doi.org/10.1021/acs.nanolett.5b01877 (2015).
21. Cheng, A., Taniguchi, T., Watanabe, K., Kim, P. & Pillet, J.-D. Guiding Dirac fermions in graphene with a carbon nanotube. *Phys. Rev. Lett.* **123**, 216804. https://doi.org/10.1103/PhysRevLett.123.216804 (2019).
22. Huang, W., Liang, S.-J., Kyoseva, E. & Ang, L. K. A new coupling mechanism between two graphene electron waveguides for ultrafast switching. *Semicond. Sci. Technol.* **33**, 035014. https://doi.org/10.1088/1361-6641/aaa595 (2018).
23. Zabolotskiy, A. D. & Lozovik, Y. E. Strain-induced pseudomagnetic field in the Dirac semimetal borophene. *Phys. Rev. B* **94**, 165403. https://doi.org/10.1103/PhysRevB.94.165403 (2016).
24. Katayama, S., Kobayashi, A. & Suzumura, Y. Pressure-induced zero-gap semiconducting state in organic conductor α-(BEDT-TTF)$_2$ I_3 salt. *J. Phys. Soc. Jpn.* **75**, 054705. https://doi.org/10.1143/JPSJ.75.054705 (2006).
25. Goerbig, M. O., Fuchs, J.-N., Montambaux, G. & Piéchon, F. Tilted anisotropic Dirac cones in quinoid-type graphene and α-(BEDT-TTF)$_2$ I_3. *Phys. Rev. B* **78**, 045415. https://doi.org/10.1103/PhysRevB.78.045415 (2008).
26. Morinari, T., Kaneshita, E. & Tohyama, T. Topological and transport properties of Dirac fermions in an antiferromagnetic metallic phase of iron-based superconductors. *Phys. Rev. Lett.* **105**, 037203. https://doi.org/10.1103/PhysRevLett.105.037203 (2010).
27. Lu, H.-Y. *et al.* Tilted anisotropic Dirac cones in partially hydrogenated graphene. *Phys. Rev. B* **94**, 195423. https://doi.org/10.1103/PhysRevB.94.195423 (2016).
28. Muechler, L., Alexandradinata, A., Neupert, T. & Car, R. Topological nonsymmorphic metals from band inversion. *Phys. Rev. X* **6**, 041069. https://doi.org/10.1103/PhysRevX.6.041069 (2016).
29. Chiu, C.-K., Chan, Y.-H., Li, X., Nohara, Y. & Schnyder, A. P. Type-II Dirac surface states in topological crystalline insulators. *Phys. Rev. B* **95**, 035151. https://doi.org/10.1103/PhysRevB.95.035151 (2017).
30. Varykhalov, A. *et al.* Tilted Dirac cone on W(110) protected by mirror symmetry. *Phys. Rev. B* **95**, 245421. https://doi.org/10.1103/PhysRevB.95.245421 (2017).
31. Tao, L. L. & Tsymbal, E. Y. Two-dimensional type-II Dirac fermions in a $LaAlO_3/LaNiO_3/LaAlO_3$ quantum well. *Phys. Rev. B* **98**, 121102. https://doi.org/10.1103/PhysRevB.98.121102 (2018).
32. Geilhufe, R. M., Commeau, B. & Fernando, G. W. Chemical-strain induced tilted Dirac nodes in (BEDT-TTF)$_2$ X_3 ($X = I, Cl, Br, F$) based charge-transfer salts. *Phys. Status Solidi Rapid Res. Lett.* **12**, 1800081. https://doi.org/10.1002/pssr.201800081 (2018).
33. Polozkov, R. G. *et al.* Carbon nanotube array as a van der Waals two-dimensional hyperbolic material. *Phys. Rev. B* **100**, 235401. https://doi.org/10.1103/PhysRevB.100.235401 (2019).
34. Zhou, X.-F. *et al.* Semimetallic two-dimensional boron allotrope with massless Dirac fermions. *Phys. Rev. Lett.* **112**, 085502. https://doi.org/10.1103/PhysRevLett.112.085502 (2014).
35. Mannix, A. J., Zhang, Z., Guisinger, N. P., Yakobson, B. I. & Hersam, M. C. Borophene as a prototype for synthetic 2D materials development. *Nat. Nanotechnol.* **13**, 444–450. https://doi.org/10.1038/s41565-018-0157-4 (2018).
36. Wang, Z.-Q., Lü, T.-Y., Wang, H.-Q., Feng, Y. P. & Zheng, J.-C. Review of borophene and its potential applications. *Front. Phys.* **14**, 33403. https://doi.org/10.1007/s11467-019-0884-5 (2019).
37. Ou, M. *et al.* The emergence and evolution of borophene. *Adv. Sci.* **8**, 2001801. https://doi.org/10.1002/advs.202001801 (2021).
38. Verma, S., Mawrie, A. & Ghosh, T. K. Effect of electron-hole asymmetry on optical conductivity in $8-Pmmn$ borophene. *Phys. Rev. B* **96**, 155418. https://doi.org/10.1103/PhysRevB.96.155418 (2017).
39. Cheng, T., Lang, H., Li, Z., Liu, Z. & Liu, Z. Anisotropic carrier mobility in two-dimensional materials with tilted Dirac cones: theory and application. *Phys. Chem. Chem. Phys.* **19**, 23942–23950. https://doi.org/10.1039/C7CP03736H (2017).
40. Islam, S. F. & Jayannavar, A. M. Signature of tilted Dirac cones in Weiss oscillations of $8-Pmmn$ borophene. *Phys. Rev. B* **96**, 235405. https://doi.org/10.1103/PhysRevB.96.235405 (2017).
41. Islam, S. F. Magnetotransport properties of $8-Pmmn$ borophene: Effects of Hall field and strain. *J. Phys. Condens. Matter*. https://doi.org/10.1088/1361-648x/aac8b3 (2018).
42. Jalali-Mola, Z. & Jafari, S. A. Tilt-induced kink in the plasmon dispersion of two-dimensional Dirac electrons. *Phys. Rev. B* **98**, 195415. https://doi.org/10.1103/PhysRevB.98.195415 (2018).
43. Zhang, S.-H. & Yang, W. Oblique Klein tunneling in $8-Pmmn$ borophene $p-n$ junctions. *Phys. Rev. B* **97**, 235440. https://doi.org/10.1103/PhysRevB.97.235440 (2018).
44. Singh, A., Ghosh, S. & Agarwal, A. Nonlinear and anisotropic polarization rotation in two-dimensional Dirac materials. *Phys. Rev. B* **97**, 205420. https://doi.org/10.1103/PhysRevB.97.205420 (2018).
45. Sengupta, P., Tan, Y., Bellotti, E. & Shi, J. Anomalous heat flow in $8-Pmmn$ borophene with tilted Dirac cones. *J. Phys. Condens. Matter*. https://doi.org/10.1088/1361-648x/aae111 (2018).

46. Yang, Z.-K., Wang, J.-R. & Liu, G.-Z. Effects of Dirac cone tilt in a two-dimensional Dirac semimetal. *Phys. Rev. B* **98**, 195123. https://doi.org/10.1103/PhysRevB.98.195123 (2018).
47. Nguyen, V. H. & Charlier, J.-C. Klein tunneling and electron optics in Dirac–Weyl fermion systems with tilted energy dispersion. *Phys. Rev. B* **97**, 235113. https://doi.org/10.1103/PhysRevB.97.235113 (2018).
48. Jalali-Mola, Z. & Jafari, S. A. Polarization tensor for tilted Dirac fermion materials: Covariance in deformed Minkowski space-time. *Phys. Rev. B* **100**, 075113. https://doi.org/10.1103/PhysRevB.100.075113 (2019).
49. Champo, A. E. & Naumis, G. G. Metal-insulator transition in 8 − *Pmmn* borophene under normal incidence of electromagnetic radiation. *Phys. Rev. B* **99**, 035415. https://doi.org/10.1103/PhysRevB.99.035415 (2019).
50. Zare, M. Negative differential thermal conductance in a borophane normal metal–superconductor junction. *Supercond. Sci. Technol.* **32**, 115002. https://doi.org/10.1088/1361-6668/ab3caf (2019).
51. Ibarra-Sierra, V. G., Sandoval-Santana, J. C., Kunold, A. & Naumis, G. G. Dynamical band gap tuning in anisotropic tilted Dirac semimetals by intense elliptically polarized normal illumination and its application to 8 − *Pmmn* borophene. *Phys. Rev. B* **100**, 125302. https://doi.org/10.1103/PhysRevB.100.125302 (2019).
52. Zhou, X. Valley-dependent electron retroreflection and anomalous Klein tunneling in an 8−*Pmmn* borophene-based *n*−*p*−*n* junction. *Phys. Rev. B* **100**, 195139. https://doi.org/10.1103/PhysRevB.100.195139 (2019).
53. Zhang, S.-H. & Yang, W. Anomalous caustics and Veselago focusing in 8−*Pmmn* borophene p–n junctions with arbitrary junction directions. *New J. Phys.* **21**, 103052. https://doi.org/10.1088/1367-2630/ab4d8f (2019).
54. Faraei, Z. & Jafari, S. A. Perpendicular Andreev reflection: Solid-state signature of black-hole horizon. *Phys. Rev. B* **100**, 245436. https://doi.org/10.1103/PhysRevB.100.245436 (2019).
55. Zare, M. Thermoelectric transport properties of borophane. *Phys. Rev. B* **99**, 235413. https://doi.org/10.1103/PhysRevB.99.235413 (2019).
56. Herrera, S. A. & Naumis, G. G. Kubo conductivity for anisotropic tilted Dirac semimetals and its application to 8−*Pmmn* borophene: Role of frequency, temperature, and scattering limits. *Phys. Rev. B* **100**, 195420. https://doi.org/10.1103/PhysRevB.100.195420 (2019).
57. Sinha, D. Spin transport and spin pump in graphene-like materials: Effects of tilted Dirac cone. *Eur. Phys. J. B* **92**, 61. https://doi.org/10.1140/epjb/e2019-90332-7 (2019).
58. Zhang, S.-H., Shao, D.-F. & Yang, W. Velocity-determined anisotropic behaviors of RKKY interaction in 8−*Pmmn* borophene. *J. Magn. Magn. Mater.* **491**, 165631. https://doi.org/10.1016/j.jmmm.2019.165631 (2019).
59. Jafari, S. A. Electric field assisted amplification of magnetic fields in tilted Dirac cone systems. *Phys. Rev. B* **100**, 045144. https://doi.org/10.1103/PhysRevB.100.045144 (2019).
60. Farajollahpour, T., Faraei, Z. & Jafari, S. A. Solid-state platform for space-time engineering: The 8−*Pmmn* borophene sheet. *Phys. Rev. B* **99**, 235150. https://doi.org/10.1103/PhysRevB.99.235150 (2019).
61. Paul, G. C., Islam, S. F. & Saha, A. Fingerprints of tilted Dirac cones on the RKKY exchange interaction in 8−*Pmmn* borophene. *Phys. Rev. B* **99**, 155418. https://doi.org/10.1103/PhysRevB.99.155418 (2019).
62. Sandoval-Santana, J. C., Ibarra-Sierra, V. G., Kunold, A. & Naumis, G. G. Floquet spectrum for anisotropic and tilted Dirac materials under linearly polarized light at all field intensities. *J. Appl. Phys.* **127**, 234301. https://doi.org/10.1063/5.0007576 (2020).
63. Sengupta, P. & Bellotti, E. Anomalous Lorenz number in massive and tilted Dirac systems. *Appl. Phys. Lett.* **117**, 223103. https://doi.org/10.1063/5.0028959 (2020).
64. Yar, A. & Ilyas, A. Effects of electric and magnetic fields on zitterbewegung of electron wave packet in borophene. *J. Phys. Soc. Jpn.* **89**, 124705. https://doi.org/10.7566/JPSJ.89.124705 (2020).
65. Jalali-Mola, Z. & Jafari, S. A. Undamped transverse electric mode in undoped two-dimensional tilted Dirac cone materials. *Phys. Rev. B* **102**, 245148. https://doi.org/10.1103/PhysRevB.102.245148 (2020).
66. Das, P., Sarkar, S. D. & Ghosh, A. K. Tunable wavevector filtering in borophane based normal metal-barrier-normal metal junctions. *J. Phys. Condens. Matter*. https://doi.org/10.1088/1361-648x/ab73a2 (2020).
67. Zheng, J., Lu, J. & Zhai, F. Anisotropic and gate-tunable valley filtering based on 8−*Pmmn* borophene. *Nanotechnology* **32**, 025205. https://doi.org/10.1088/1361-6528/abbbd7 (2020).
68. Farajollahpour, T. & Jafari, S. A. Synthetic non-Abelian gauge fields and gravitomagnetic effects in tilted Dirac cone systems. *Phys. Rev. Res.* **2**, 023410. https://doi.org/10.1103/PhysRevResearch.2.023410 (2020).
69. Rostami, H. & Juričić, V. Probing quantum criticality using nonlinear Hall effect in a metallic Dirac system. *Phys. Rev. Res.* **2**, 013069. https://doi.org/10.1103/PhysRevResearch.2.013069 (2020).
70. Kapri, P., Dey, B. & Ghosh, T. K. Valley caloritronics in a photodriven heterojunction of Dirac materials. *Phys. Rev. B* **102**, 045417. https://doi.org/10.1103/PhysRevB.102.045417 (2020).
71. Faraei, Z. & Jafari, S. A. Electrically charged Andreev modes in two-dimensional tilted Dirac cone systems. *Phys. Rev. B* **101**, 214508. https://doi.org/10.1103/PhysRevB.101.214508 (2020).
72. Zhou, X. Anomalous Andreev reflection in an 8−*Pmmn* borophene-based superconducting junction. *Phys. Rev. B* **102**, 045132. https://doi.org/10.1103/PhysRevB.102.045132 (2020).
73. Zhou, X. Valley splitting and anomalous Klein tunneling in borophane-based *n*−*p* and *n*−*p* − *n* junctions. *Phys. Lett. A* **384**, 126612. https://doi.org/10.1016/j.physleta.2020.126612 (2020).
74. Li, J., Xu, T., Zhu, G.-B. & Pan, H. Photoinduced anomalous Hall and nonlinear Hall effect in borophene. *Solid State Commun.* **322**, 114092. https://doi.org/10.1016/j.ssc.2020.114092 (2020).
75. Napitu, B. D. Photoinduced Hall effect and transport properties of irradiated 8 − *Pmmn* borophene monolayer. *J. Appl. Phys.* **127**, 034303. https://doi.org/10.1063/1.5130025 (2020).
76. Li, J., Sun, Y., Wu, M. & Pan, H. Novel electric field effects on magneto-optical conductivity in eight−*Pmmn* borophene. *J. Phys. Condens. Matter*. https://doi.org/10.1088/1361-648x/abf19e (2021).
77. Mojarro, M. A., Carrillo-Bastos, R. & Maytorena, J. A. Optical properties of massive anisotropic tilted Dirac systems. *Phys. Rev. B* **103**, 165415. https://doi.org/10.1103/PhysRevB.103.165415 (2021).
78. Kong, Z., Li, J., Zhang, Y., Zhang, S.-H. & Zhu, J.-J. Oblique and asymmetric Klein tunneling across smooth NP junctions or NPN junctions in 8 − *Pmmn* borophene. *Nanomaterials***11**, https://doi.org/10.3390/nano11061462 (2021).
79. Tan, C.-Y., Yan, C.-X., Zhao, Y.-H., Guo, H. & Chang, H.-R. Anisotropic longitudinal optical conductivities of tilted Dirac bands in $1T^{'} - Mo S_2$. *Phys. Rev. B*. https://doi.org/10.1103/PhysRevB.103.125425 (2021).
80. Željana, B. L. Effects of the Dirac cone tilts on coupled plasmon modes in electron systems with different dimensionalities. *Physica B* **615**, 413124. https://doi.org/10.1016/j.physb.2021.413124 (2021).
81. Xu, Y. & Zhou, X. Light-modulated anisotropic Andreev reflection across an 8 − *Pmmn* borophene-based superconducting junction. *Res. Phys.* **27**, 104523. https://doi.org/10.1016/j.rinp.2021.104523 (2021).
82. Fu, W., Ke, S.-S., Lu, M.-X. & Lü, H.-F. Coulomb bound states and atomic collapse in tilted Dirac materials. *Physica E* **134**, 114841. https://doi.org/10.1016/j.physe.2021.114841 (2021).
83. Jalali-Mola, Z. & Jafari, S. A. Tilt-induced many-body corrections to optical conductivity of tilted Dirac cone materials. *Phys. Rev. B* **104**, 085152. https://doi.org/10.1103/PhysRevB.104.085152 (2021).
84. Pattrawutthiwong, E., Choopan, W. & Liewrian, W. Possible verification of tilt mismatch in asymmetric Dirac-cone systems using resonant tunneling properties. *Phys. Lett. A* **393**, 127154. https://doi.org/10.1016/j.physleta.2021.127154 (2021).

85. Li, D. *et al.* 2d boron sheets: Structure, growth, and electronic and thermal transport properties. *Adv. Funct. Mater.* **30**, 1904349. https://doi.org/10.1002/adfm.201904349 (2020).
86. Yesilyurt, C. *et al.* Electrically tunable valley polarization in Weyl semimetals with tilted energy dispersion. *Sci. Rep.* **9**, 1–16. https://doi.org/10.1038/s41598-019-40947-2 (2019).
87. Nakhaee, M., Ketabi, S. A. & Peeters, F. M. Tight-binding model for borophene and borophane. *Phys. Rev. B* **97**, 125424. https://doi.org/10.1103/PhysRevB.97.125424 (2018).
88. Turbiner, A. V. Quantum mechanics: Problems intermediate between exactly solvable and completely unsolvable. *Sov. Phys. JETP* **94**, 33–44 (1988).
89. Bender, C. M. & Boettcher, S. Quasi-exactly solvable quartic potential. *J. Phys. A Math. Gen.* **31**, L273–L277. https://doi.org/10.1088/0305-4470/31/14/001 (1998).
90. Downing, C. A. On a solution of the Schrödinger equation with a hyperbolic double-well potential. *J. Math. Phys.* **54**, 072101. https://doi.org/10.1063/1.4811855 (2013).
91. Hartmann, R. R. Bound states in a hyperbolic asymmetric double-well. *J. Math. Phys.* **55**, 012105. https://doi.org/10.1063/1.4861938 (2014).
92. Hartmann, R. R. & Portnoi, M. E. Exciton states in narrow-gap carbon nanotubes. *AIP Conf. Proc.* **1705**, 020046. https://doi.org/10.1063/1.4940294 (2016).
93. Hartmann, R. R. & Portnoi, M. E. Pair states in one-dimensional Dirac systems. *Phys. Rev. A* **95**, 062110. https://doi.org/10.1103/PhysRevA.95.062110 (2017).
94. Ushveridze, A. *Quasi-Exactly Solvable Models in Quantum Mechanics* (CRC Press, Boca Raton, 2017).
95. Rycerz, A., Tworzydło, J. & Beenakker, C. Valley filter and valley valve in graphene. *Nat. Phys.* **3**, 172–175. https://doi.org/10.1038/nphys547 (2007).
96. Žutic, I., Fabian, J. & Das Sarma, S. Spintronics: Fundamentals and applications. *Rev. Mod. Phys.* **76**, 323–410. https://doi.org/10.1103/RevModPhys.76.323 (2004).
97. Vitale, S. A. *et al.* Valleytronics: Opportunities, challenges, and paths forward. *Small* **14**, 1801483. https://doi.org/10.1002/smll.201801483 (2018).
98. Clemence, D. P. Low-energy scattering and Levinson's theorem for a one-dimensional Dirac equation. *Inverse Probl.* **5**, 269–286. https://doi.org/10.1088/0266-5611/5/3/005 (1989).
99. Lin, Q.-G. Levinson theorem for Dirac particles in one dimension. *Eur. Phys. J. D* **7**, 515–524. https://doi.org/10.1007/s100530050379 (1999).
100. Calogeracos, A. & Dombey, N. Strong Levinson theorem for the Dirac equation. *Phys. Rev. Lett.* **93**, 180405. https://doi.org/10.1103/PhysRevLett.93.180405 (2004).
101. Ma, Z.-Q., Dong, S.-H. & Wang, L.-Y. Levinson theorem for the Dirac equation in one dimension. *Phys. Rev. A* **74**, 012712. https://doi.org/10.1103/PhysRevA.74.012712 (2006).

Acknowledgements

This work was supported by the EU H2020 RISE projects TERASSE (H2020-823878) and DiSeTCom (H2020-823728). RAN is funded by the DOST-SEI ASTHRDP program. AW is supported by a UK EPSRC PhD studentship (Ref. 2239575) and by the NATO Science for Peace and Security project NATO.SPS.MYP.G5860. RRH acknowledges financial support from URCO (14 F 1TAY20-1TAY21). The work of MEP was supported by the Russian Science Foundation (Project No. 20-12-00224).

Author contributions

All authors contributed equally to the writing of the manuscript.

Competing interests

The authors declare no competing interests.

Additional information

Supplementary Information The online version contains supplementary material available at https://doi.org/10.1038/s41598-022-11742-3.

Correspondence and requests for materials should be addressed to R.R.H.

Reprints and permissions information is available at www.nature.com/reprints.

Publisher's note Springer Nature remains neutral with regard to jurisdictional claims in published maps and institutional affiliations.